Microstructure of high modulus solid state extruded polyethylene: 2. X-ray scattering studies of 12, 24 and 36 extrusion draw ratio

W. Wade Adams, Robert M. Briber, Edward S. Sherman, Roger S. Porter and Edwin L. Thomas*

Polymer Science and Engineering Department, University of Massachusetts, Amherst, Massachusetts 01003, USA

(Received 12 December 1983; revised 18 April 1984)

Dedicated to Dr Anton Peterlin on the occasion of his 75th birthday

The microstructure of a series of solid state extruded polyethylene fibres was examined by wide- and small-angle X-ray scattering. By measuring absolute intensities using a two dimensional position sensitive detector, accurate values of the small-angle invariant for anisotropic samples were obtained. This measurement coupled with wide-angle X-ray scattering and d.s.c. permitted determination of the density of the noncrystalline component. The use of a two phase model for solid state extruded polyethylene is justified if consideration is given to the effective densities of the crystalline and noncrystalline phases, which change with deformation. The effective density of the crystalline phase decreases by 1% (0.999–0.990 g cm^{-3}) from the unextruded billet compared to a 36 draw ratio extrudate, while the noncrystalline phase density increases by 6% (0.84–0.89 g cm^{-3}). These changes lead to an overall decrease in the mean squared electron density fluctuation of 63%. The average axial crystallite length measured by wide-angle X-ray scattering increases with extrusion draw ratio while the SAXS long period decreases and weakens considerably. These observations and the electron microscopy results from the previous paper, (*Polymer*, 1982, **23**, 1069), are fully consistent with the key features of the Peterlin model of fibre microstructure.

(Keywords: high modulus; solid state extrusion; small-angle X-ray scattering; invariant; fibre microstructure)

INTRODUCTION

The application of the solid state extrusion (SSE) method to various thermoplastics has produced high modulus ultradrawn fibres and films with remarkable properties[1,2]. Samples produced by this technique, along with related methods such as hydrostatic extrusion, have been extensively studied (especially high density polyethylene) but the detailed microstructural picture is still not complete[3,4]. Recently Kanamoto[5] obtained an axial tensile modulus near that of the theoretical crystal modulus of polyethylene (222 GPa vs. 240–340 GPa)[6,7] by post drawing of a solid state extruded single crystal mat formed from ultrahigh molecular weight polyethylene (UHMWP). This achievement of properties by chain orientation and extension in the solid state reinforces the need for more thorough understanding of the process and the resultant morphology of the materials.

Prior microstructural studies of the solid state extrusion process polymers have revealed the nature of the initial deformation of spherulitic material into a highly oriented fibrillar texture[3,8–14]. For linear polyethylene (PE), an extrusion draw ratio (EDR) of 6–12 is sufficient for the transformation which is accompanied by drastic changes in the birefringence, crystallite orientation, and long period, as well as tensile modulus and strength. For higher EDR, properties such as tensile modulus and axial crystallite size continue to change, while crystallite orientation, birefringence and noncrystalline chain mobility reach a plateau in the range of 15 EDR[14–16]. Changes in other properties are variable: for example the long period has been reported to either increase[12], decrease[2,9,10,13,16] or remain nearly constant[14], and its intensity decreases[3,9,14,16] or disappears altogether[17] with increasing EDR, depending upon the details of the extrusion process (pressure, temperature, extrusion rate, molecular weight).

Some models (see *Figure 1* in Part 1 of this work[18]) of the fibrillar structure which account for the increase in tensile modulus with increasing deformation rely heavily on the long period measured by small-angle X-ray scattering[19,20]. It is therefore worthwhile to critically assess the small-angle X-ray scattering from SSE fibres in view of the cited variable long period behaviour.

The variation of the SAXS intensity with increasing polymer deformation has included measures by visual estimation[20], peak height[21–23], peak area[24–27] and 'intensity per unit volume'[3], none of which by themselves permit fundamental interpretation. The integrated intensity or invariant has seldom been measured, and then only by film or one-dimensional detector methods[28–32]. Since the small angle scattering from a fibre (or any other oriented system) is anisotropic, the proper integration of the scattered intensity requires two-dimensional digital recording which will also enable determination of other useful information, including macrolattice size and macrolattice distortion from the breadth of the long period peak(s), the anisotropy of the electron density fluctuations and the specific surface area between the crystalline and noncrystalline phases. In addition, the

* To whom correspondence should be sent

0032-3861/85/010017-10$03.00

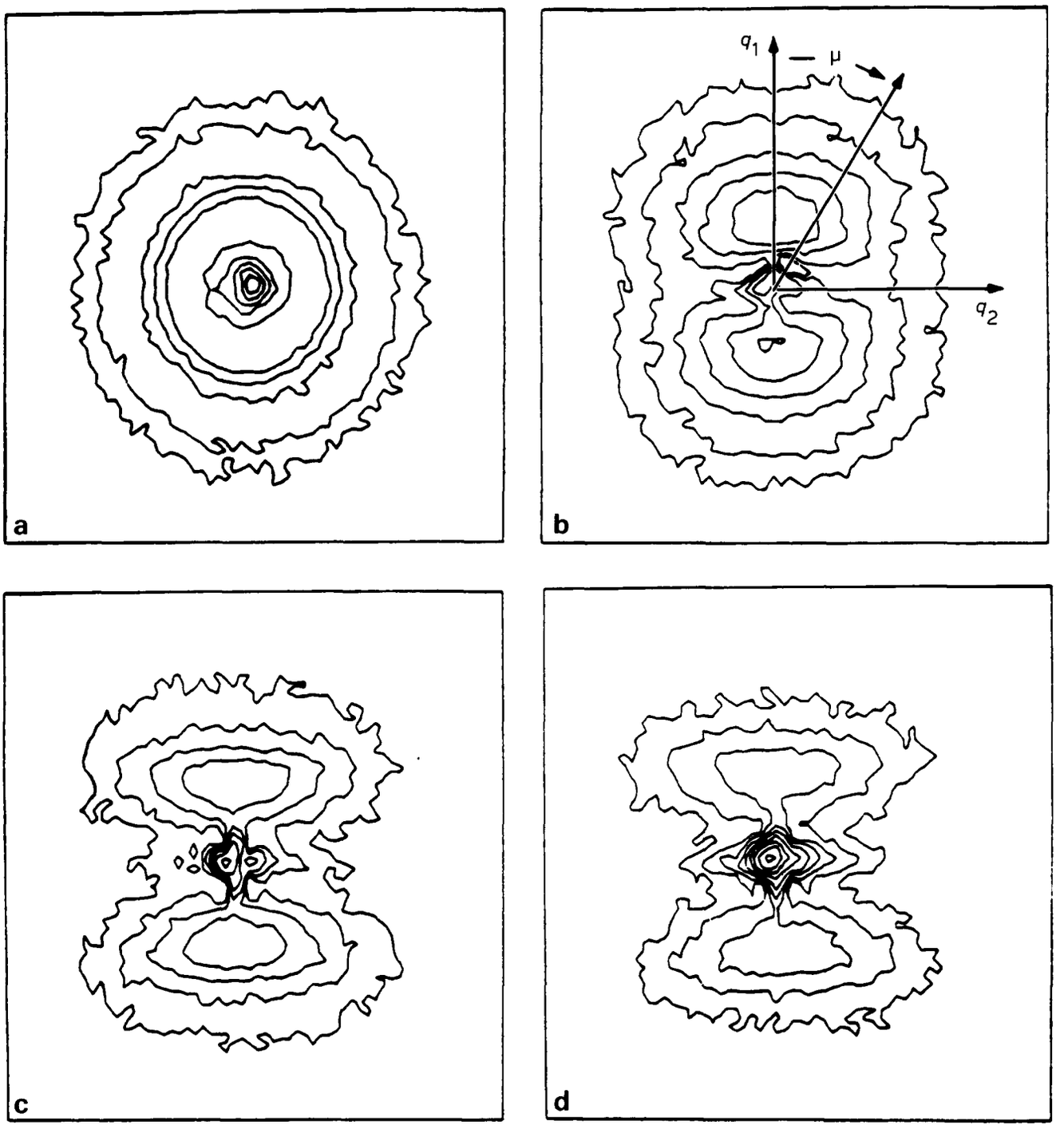

Figure 1 SAXS isointensity contour plots at 5 m geometry for (a) initial billet, 1 EDR and (b) 12 EDR, (c) 24 EDR and (d) 36 EDR samples. Data are normalized for sample volume and incident beam intensity, outer contour at 16 counts, each inner contour increases by a factor of 2. Void scattering at the centers of the patterns was not included in the invariant calculations. Scattering vectors q_1 and q_2 and azimuthal angle μ are indicated on (b)

integrated intensity, placed on an absolute scale yields the mean squared electron density fluctuation which when coupled with data on degree of crystallinity and crystal density, allows the determination of the effective non-crystalline phase density, a parameter that should prove useful in understanding the deformation process during solid state extrusion and help distinguish among the proposed microstructural models.

In Part 1 of this study[18], electron microscopy was used to determine the microstructure of a series of solid state extruded polyethylene fibres. Microfibres composed of alternating crystalline and noncrystalline regions formed ribbon-like aggregates, and the axial crystallite size increased with increasing extrusion draw ratio. In the 36 EDR sample, the crystal size distribution was broad, with a small component of very long crystals (1000–8000 Å). Aligned diffracting crystallite colonies observed in dark field images indicated coherence of sequences of adjacent crystallites along the fibre, imparted by needle crystals or thin crystalline bridges. At these high draw ratios, the tensile moduli of extruded materials is likely to be controlled by the size and amount of the long crystals and the number and type of bridges between shorter crystals.

Table 1 Properties of solid state extruded polyethylene samples

Extrusion draw ratio	Tensile modulus	D.s.c. degree of crystallinity	Density g cm^{-3}
EDR	GPa	ϕ_c	$\overline{\rho}$
1	≈1	77	0.965
12	10	73	0.968
24	27	82	0.974
36	40	83	0.975

In the study detailed in this paper we employed small and wide-angle X-ray scattering to investigate the nature of the regions along the microfibres between the crystals, and in particular, the *noncrystalline phase density* as well as the axial crystal coherence and fibre long period.

SAMPLES

Details of the sample preparation by solid state extrusion have been presented in a previous paper[18]. Sample designation and some properties are listed in *Table 1*. Re-examination of the higher molecular weight sample from Part 1 of this study revealed significant preferred orientation in the starting billet, making the final draw ratio uncertain. Only the lower molecular weight polyethylene (Alathon 7050) will be considered in this paper.

EXPERIMENTAL METHODS

Wide-angle X-ray scattering

Profiles of the (002) reflection were recorded using a Siemens D500 wide angle diffractometer employed in the symmetric transmission mode with Ni filtered CuKα radiation. The beam divergence was minimized for line broadening measurements with 0.1° incident beam slits and a 0.018° receiving slit so that a 1.5 mm thick hexamethylene tetramine standard had an integral breadth $\Delta\beta_{instr.}$ of 0.13° for a reflection at $2\theta = 76.73°$.

The PE sample profiles were recorded over a 2θ angular range of 5° starting from 73° at a rate of 0.1° min^{-1}. The count rate at the main peak was typically 150 counts s^{-1}. The background was found to be constant (~3–5 counts s^{-1}) on both sides of the peak. The Rachinger correction was applied to remove the CuKα_2 peak from the (002) profile[33]. Integral breadths, $\Delta\beta_{obs}$, were calculated from the corrected profiles by

$$\Delta\beta_{obs} = \frac{1}{I_{max}} \int I(2\theta)\mathrm{d}(2\theta) \tag{1}$$

where I_{max} is the maximum peak intensity.

The correction of the observed integral breadths for instrumental broadening depends on whether the peak shapes are Cauchy or Gaussian[34]. If the profiles are Cauchy:

$$\Delta\beta_{obs} = \Delta\beta_L + \Delta\beta_{instr.} \tag{2}$$

while for Gaussian profiles:

$$\Delta\beta^2_{obs} = \Delta\beta^2_L + \Delta\beta^2_{instr.} \tag{3}$$

where $\Delta\beta_L$ is the broadening from the sample. Since the observed peaks are generally represented by a combination of Cauchy and Gaussian functions we have calculated the mean crystal size for both cases using the Scherrer equation:

$$l_c^{002} = \frac{K\lambda}{\Delta\beta_L \cos\theta} \tag{4}$$

where $K = 1.0$ for $00l$ reflections[35].

Precise measurement of the (200), (020) and (002) d-spacings was made using the Kα_1 peak after applying the Rachinger correction. Quartz was used to calibrate the 2θ values.

Orientation measurements were made from microdensitometer traces (Optronics Photoscan P-2000) of flat film photographs made on a Statton type (Warhus) camera with CuKα radiation from an Elliot GX20 Rotating Anode Generator. The azimuthal angle of arcing where the intensity of a reflection decreased to half its maximum value was taken as a measure of orientation.

Small-angle X-ray scattering

Small-angle X-ray scattering was performed at the National Center for Small Angle Scattering Research (NCSASR) at Oak Ridge National Laboratories, Oak Ridge, Tennessee, using the 10 m camera (details of this facility are given in ref. 36). The pinhole collimation and two dimensional position sensitive detector makes this instrument useful for studying the anisotropic scattering from fibres. The CuKα X-ray source was monochromated by pyrolitic graphite in the incident beam. Incident beam intensity was calibrated with a series of nickel foils[37]. Specimen transmittance was measured by comparing the small angle scattering of a standard (Lupolen) to its scattering with the beam attenuated by the sample placed in front of the first collimation pinhole.

Extruded PE samples are visually transparent, indicating the absence of heterogeneities larger than about 0.1 μm. Samples were trimmed to approximately 1 mm thickness and were greater than 1 mm wide so that the incident 1 mm × 1 mm X-ray beam was completely covered by sample. Data were collected at specimen to detector distances of 5.15 m, 2.20 m and 1.12 m encompassing a scattering vector range from 0.00122–0.488 Å^{-1}. Data from the samples (mounted with the fibre direction vertical) was collected for a time sufficient to give ~3% counting statistical error after correction for electronic noise, parasitic scattering, and detector sensitivity.

The integrated intensity, of Porod invariant (Q)[38] is of the form

$$Q = \mathrm{Const.} \int_0^\infty \int_0^\infty I(q_1, q_2) q_2 \mathrm{d}q_1 \mathrm{d}q_2 \tag{5}$$

assuming cylindrical symmetry about the fibre direction q_1. A computer program to perform this integration was written for use at ORNL*[39]. The mean squared electron density fluctuation can be written:

$$\langle(\rho - \bar{\rho})^2\rangle = \frac{Q}{i_e N^2 t \lambda^3 I_0 a} \tag{6}$$

where i_e is the Thomson cross-section of a free electron

*The program 'INVAR' is available at the ORNL NCSASR.

Table 2 WAXS data (Å)

Extrusion draw ratio EDR	d_{200}	d_{020}	d_{002}	ρ_c' g cm^{-3}	δ^{β}_{002}	I_c^{002} G* C*	Azimuthal orientation half-angle (110)
1	3.707	2.471	1.273	0.999	0.529°	220–260	360°
12	3.717	2.469	1.272	0.997	0.426°	260–340	17°
24	3.726	2.467	1.272	0.995	0.448°	260–320	6°
36	3.735	2.471	1.273	0.990	0.357°	330–470	5°

* G = Gaussian profile, C = Cauchy profile

(7.9×10^{-26} cm^2), N is Avogadro's number, t is the specimen thickness, a is the specimen–detector distance and I_0 is the normalized total incident intensity measured in absolute units[40].

By subtracting from the measured scattered intensity the liquid scatter contribution (Fl) arising from density fluctuations within each phase, the mean squared electron density fluctuation measured then arises only from the electron density difference between the phases, independent of the number of phases or the nature of the phase boundaries. For a semicrystalline polymer, the usual two-phase, sharp boundary approximation yields

$$\langle(\rho-\bar{\rho})^2\rangle=(\rho_c'-\rho_a')^2\phi_c\phi_a \tag{7}$$

where ϕ_c and ϕ_a are the volume fractions of the crystalline and noncrystalline phases, respectively. Note that ρ_c' and ρ_a' represent the actual average densities of the two phases for the particular deformation state. Thus, one anticipates the initial crystal density ρ_c to be reduced by defects to ρ_c' and the noncrystalline density ρ_a to be increased by the drawing to ρ_a'. As first shown by Fischer[29,41], combining an independent measure of $\bar{\rho}$ (the bulk sample density) with an accurate measure of ρ_c' from wide-angle X-ray scattering enables the value of ρ_a' to be determined:

$$\rho_a'=\bar{\rho}-\frac{\langle(\rho-\bar{\rho})^2\rangle}{(\rho_c'-\bar{\rho})} \tag{8}$$

The accurate measurement of the liquid scattering (Fl) can be obtained by a Porod law analysis at high scattering angles. The dependence of the scattered intensity from oriented assemblies of anisotropic articles at large q is given by[43]:

$$I(q,\mu)=\frac{K_p(\mu)}{q^4}+Fl(\mu) \tag{9}$$

The azimuthal angle μ is indicated in *Figure 1*, such that $Fl(\mu)$ can be determined from plots of q^4I *versus* q^4 at various azimuthal angles. Subtraction of the liquid scattering from the scattered intensity was performed by sectors ($0°<\mu\leqslant 22.5°$, $22.5°<\mu\leqslant 67.5°$ and $67.5°<\mu\leqslant 90°$) assuming $Fl(\mu)$ was independent of scattering angle within each sector.

Porod law analysis also gives Porod constants (K_p) from the intercepts on the q^4I vs. q^4 plots. K_p can be used for isotropic systems to give the surface-to-volume ratio[43], or for anisotropic systems, $K_p(\mu)$ can be interpreted as relative sizes and shapes of oriented ellipsoids of revolution[42].

RESULTS

Wide-angle X-ray diffraction

The uncorrected integral breadths of the (002) reflections are given in *Table 2*. Since the observed peak profiles are neither Gaussian nor Cauchy, calculated values of crystal size were made for both cases and are also listed in *Table 2*. Since there are no detectable higher order (00l) reflections, no correction can be made for possible strain and paracrystalline line broadening contributions, and hence the values listed are *lower bounds* on crystal thickness. A strong increase in the axial crystal coherence length is observed with EDR, rising from 240 Å for the billet to 400 Å for the 36 EDR sample.

The (200), (020) and (002) spacings are also listed in *Table 2*. The effect of increasing draw ratio is to increase the a axis spacing with essentially no change in the dimensions of the b and c axes. The expansion of the a axis causes the unit cell density to drop by about 1% from the billet (0.999 g cm^{-3}) to the most highly drawn 36 EDR sample (0.990 g cm^{-3}).

The crystallite orientation increases with increasing draw ratio. Wide-angle flat film X-ray diffraction patterns had half-angle azimuthal spreads of 17°, 6° and 5° for (110) for the 12, 24 and 36 EDR samples, respectively. This increase in orientation agrees with our earlier electron diffraction results[18] showing that the c-axis orientation increases greatly up to EDR 24 but only slightly thereafter. These values also agree with spectroscopic orientation data which gave chain axis misorientation angles of 17°, 6° and <2°[43,51].

Small-angle X-ray scattering

Figure 1 shows isointensity contour plots for the long geometry (sample-to-detector distance, 5.15 m) for all the extrudates. The data has been background corrected and normalized with respect to incident beam intensity and sample thickness. Contour line intervals are at multiples of 2^n counts with the outside line representing 16 counts. All samples show a two point pattern of intensity on the meridian similar to that observed for conventionally drawn fibres[44,45]. The long period calculated by applying Bragg's law to the position of the peak intensity maximum is given in *Table 3*.

A plot of the intensity vs. 2θ along q_1 enables the meridional integral breadth ($\Delta\beta_1$) to be obtained and is given by:

$$\Delta\beta_1=\frac{2}{I(q_1^*,0)}\int_{q_1^*}^{\infty} I(q_1,0)\mathrm{d}q_1 \tag{10}$$

Table 3 Comparison of crystallite sizes and long periods (Å)

Extrusion draw ratio EDR	l_cDF	l_c^{002} [a]	l_sLAM[b]	LSAXS	l_c^{002}/LSAXS
1	–	240	–	279[c]	0.86
12	270	300	230	349	0.86
24	270	290	175	266	1.09
36	390	400	150	237	1.69

[a] Values listed are mean of Cauchy and Gaussian values from Table 2
[b] From ref. (51)
[c] Lorentz corrected long period

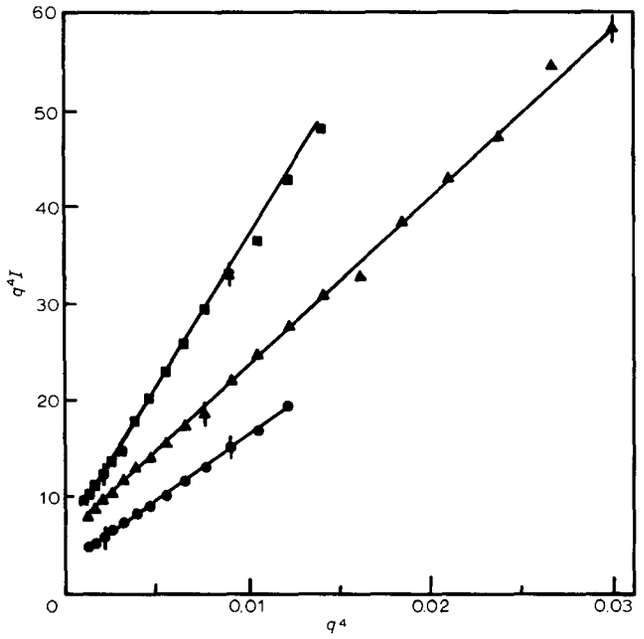

Figure 2 Porod plot for 36 EDR sample at three azimuthal angles (μ). Lines are least squares fits to Porod's Law, equation (9). (●): μ=0°C; (▲): μ=45°C; (■): μ=90°C

Similarly, the average width of the microfibres may be measured from the integral breadth of the peak in the q_2 direction by:

$$\Delta\beta_2 = \frac{1}{I(q_1^*,0)} \int_{-\infty}^{+\infty} I(q_1^*,q_2)\mathrm{d}q_2 \qquad (11)$$

where q_1^*,0 is the position of the intensity maximum. The integral breadths along q_1 (5.1, 4.3 and 4.4 mrad for 12, 24, 36 EDR) are much smaller than along q_2 (7, 10, 12 mrad for 12, 24, 36 EDR).

The constancy of integral breadth $\Delta\beta_1$ along the meridional direction indicates little net change in the three contributing factors (size, size distribution and paracrystalline distortion) to macrolattice line breadth with deformation. The integral breadth of the SAXS peak perpendicular to the fibres, $\Delta\beta_2$, can be interpreted in terms of microfibril radii by equation (12):

$$\langle R\rangle = \frac{0.52\lambda}{\Delta\beta_2} \qquad (12)$$

where $\langle R\rangle$ is the ratio between the 4th and 3rd moments of the microfibril radius distribution function[46]. $\Delta\beta_2$ increases proportionally to EDR, indicating a thinning of the microfibres ($\langle R\rangle$ decreases from 103 to 80 to 64 Å), which was also observed by bright field electron microscopy and wide-angle X-ray diffraction. It is interesting to note that $\langle R\rangle$ obeys Peterlin's[47] prediction that the diameter of the microfibres follows a $\lambda^{-1/2}$ dependence.

The evaluation of $\langle(\rho-\bar{\rho})^2\rangle$ for an anisotropically scattering specimen requires considerably more effort than for an isotropic specimen. The two-dimensional integration (equation (5)) requires data collection at the 1, 2 and 5 m geometries. Complete details of the invariant calculation using a two-dimensional position sensitive detector system for samples possessing cylindrically symmetric scattering patterns are presented elsewhere[39]. The main features pertinent here are the verification of the two-phase, sharp boundary approximation and the separation and subtraction of the orientation dependent density fluctuation scattering component.

The assumption of sharp interfaces between phases which is inherent is equation (7), was experimentally verified by Porod plots. *Figure 2* shows plots of q^4I vs. q^4 for the 36 EDR sample. The straight line between the individual points is a least squares fit to the data by equation (9), so that $Fl(\mu)$ is the slope and $K_p(\mu)$ is the intercept for each value of μ. Porod's Law was found to be obeyed over the range of scattering angles from approximately q=0.2 Å^{-1} (2θ=2.8°) to q=0.3 Å^{-1} (2θ=4.2°) except for μ=45°, where a linear fit was possible to q=0.42 Å^{-1} (2θ=5.9°).

Table 4 gives the values of $Fl(\mu)$ along the meridian (μ=0°), at 45° to the meridian and along the equator (μ=90°). Significant anisotropy in Fl occurs, for example in the 36 EDR sample, the intensity at 90° is nearly three times that at 0°, as can be clearly seen in the high angle regions of the isointensity plots in *Figure 3*.

The Porod constants $K_p(\mu)$ listed in *Table 4* are also anisotropic. In addition, there are significant increases in K_p at all EDR over the undrawn isotropic values. The anisotropy is the most pronounced for samples of 24 and 36 EDR, with an almost 2:1 ratio of the liquid scatter intensity along μ=90° *versus* 0°. The specific surface (S/V) can be calculated for isotropic samples from the Porod constant by[38]

$$S/V = \frac{K_p}{2\pi(\Delta\rho)^2} \qquad (13)$$

The specific surface of the billet is 7.87×10^{-3} Å^{-1}. Measured values for the mean square electron density fluctuation are given in *Table 5*, along with the degree of crystallinity and effective crystal density used in equations

Table 4 Anisotropic Porod analysis

	$F/(\mu)$ (electrons^2/Å^3)			$10^5 K_p$ (electrons^2/Å^7)		
μ	0°	45°	90°	0°	45°	90°
Extrusion draw ratio EDR						
1	0.14			13		
12	0.12	0.12	0.16	20	34	23
24	0.069	0.091	0.15	17	32	31
36	0.064	0.093	0.16	18	25	29

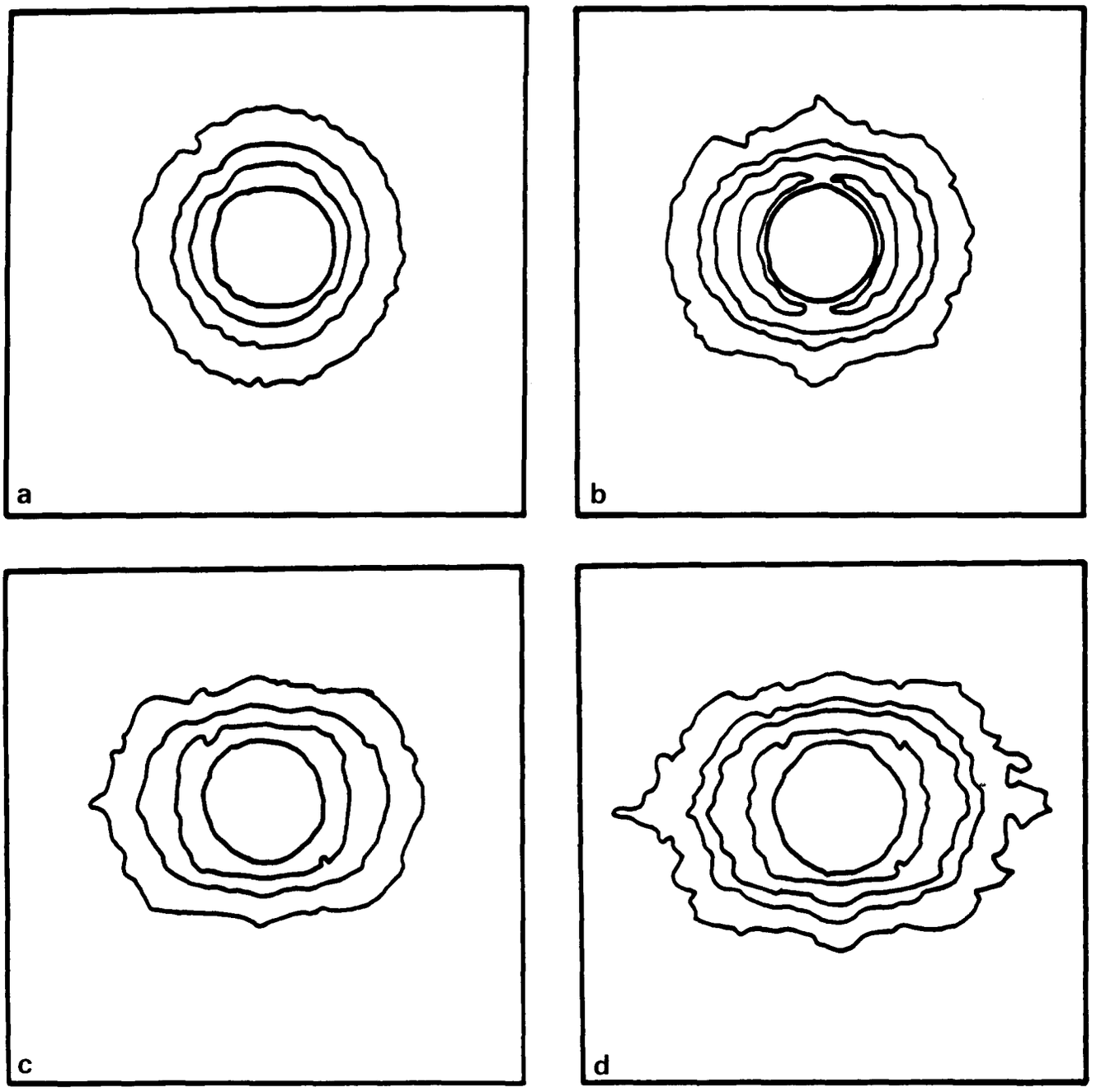

Figure 3 Isointensity contour plots for data taken at 1 m geometry (fibre direction vertical). Round 'holes' in centres are due to the use of a large (≈6 cm diameter) beam stop to block the interference peak, avoiding counter overflow during the long (~20 h) run times

Table 5 Small-angle X-ray scattering

Extrusion draw ratio EDR	$\langle(\rho-\bar{\rho})^2\rangle$ (mole e$^-$ cm^{-3})^2	ϕ_c	ρ_c' (g cm^{-3})	ρ_a' (g cm^{-3})
1	1.43×10^{-3}	0.77	0.999	0.84
12	0.673×10^{-3}	0.73	0.997	0.88
24	0.668×10^{-3}	0.82	0.995	0.88
36	0.529×10^{-3}	0.83	0.990	0.89

(7) and (8) to calculate the effective noncrystalline region density.

DISCUSSION

Previously, dark field electron microscopy was used to directly image the crystalline regions to investigate their distribution of sizes and shapes[18]. Two additional methods have now been applied to study crystal size and connectivity therefore permitting a test of the various morphological models for the structure of solid state extruded PE. Wide-angle X-ray diffraction line breadth analysis measures the weight average axial crystal size from coherently scattering (002) lattice planes. Measurement of *d*-spacings by WAXS yields the crystalline phase density and WAXS azimuthal arcing gives the orientation of the crystalline regions. SAXS will reveal a long period if the crystals exist within periodic macrolattices but most importantly, SAXS permits calculation of the density difference between the crystalline and noncrystalline regions from the invariant. Both X-ray diffraction techniques average over several (mm)^3 of bulk sample while electron microscopy is highly specific to relatively small fields of view (≈ 10 μm in diameter) of thin regions of the detached microfibres. Although differing in moment (weight vs. number average) and sensitivity, a combined synthesis of the observed quantities reveals important measures of crystal order and connectivity via the intervening noncrystalline regions.

The value of the long period for the undeformed billet, 279 Å (Lorentz corrected), is significantly less than that for the 12 EDR material (349 Å) and is dependent on the billet preparation conditions (temperature and pressure). Further drawing considerably decreases L, to 266 Å and 237 Å for 24 and 36 EDR, respectively. This decrease of L with increasing draw has been previously reported for SSE PE[2,9,10,13,16] and is at variance with other reports where L is either not affected much by drawing[14] or even increases[12]. The initial increase in L (280–350 Å) is accompanied by a decrease of sample crystallinity from 77% to 73%. On further deformation the crystalline volume fraction increases to 83%.

The fluctuation scattering can be measured by determining the absolute small-angle scattering intensity at high scattering angles. This weak scattering, arising from spatial and temporal density fluctuations in both the crystalline and amorphous phases, can be written for an oriented system as:

$$Fl(T,\mu)=\phi_a Fl_a(T,\mu)+\phi_c Fl_c(T,\mu) \qquad (14)$$

The magnitude of the fluctuation scattering is directly proportional to the amounts of the phases present. The measured value of the total electron density fluctuation for the undrawn billet, 0.14 e^2/Å^3, is 50% higher than the calculated value of 0.095 e^2/Å^3 using Ruland and Rathje's[48] values of 0.22 e^2/Å^3 for Fl_a and 0.058 e^2/Å^3 for Fl_c and the measured sample ϕ_c of 0.77. For the undrawn material, the density fluctuations are isotropic, due to both the Fl_c term (mostly from phonons) and to Fl_a (from defects), which are randomly oriented. However, Fl exhibits strong anisotropy for the extrudates. The temperature and orientation dependence of Fl for a drawn ($\lambda=4$) high density polyethylene has been examined by Wiegand and Ruland[49]. They found that for this modestly drawn PE sample, the anisotropy in Fl was essentially due to the oriented crystals. We find at 12 EDR a weakly orientation dependent Fl, but by 24 EDR the scattered intensity along the meridian is less than half that along the equator. This anisotropy in Fl is more pronounced at 36 EDR.

The specific surface calculated from the Porod constant for the initial billet, 7.87×10^{-3} (Å^{-1}), is in agreement with the simple estimate of S/V based on the long period ($2/L=7.17 \times 10^{-3}$ (Å^{-1})) supporting the picture of a periodic lamellar structure for the undeformed billet. The calculated noncrystalline phase density for the initial undeformed polyethylene billet, 0.84 g cm^{-3}, is reasonable, compared to estimates from dilatometric melt density extrapolations[30], and other previous SAXS measurements for polyethylene[29]. It is also consistent with the enthalpic degree of crystallinity, the wide-angle X-ray crystal density, and the experimental bulk density for the billet (i.e. $\rho_{calc}=[(0.77)(0.999)+(0.23)(0.84)]=0.962$ *versus* 0.965 measured). For the extrudates, current theory does not provide a quantitative interpretation to the magnitude of $K_p(\mu)$ in terms of a surface to volume ratio. However, it is notable that the Porod constants for $\mu=90°$ increase with draw ratio, consistent with the thinning of the microfibres.

The dark field crystal size and distribution, and the wide-angle X-ray scattering average crystal size are model independent and provide direct measures of the crystalline coherence. Both these techniques provide lower limits to the actual average crystal sizes. The longitudinal acoustic mode determined-average stem length (l_c^{LAM}) does not differentiate between extended chains in crystals or other all-*trans* chain sequences, such as taut tie molecules. The decrease in the SAXS interference peak intensity indicates the amount of periodic material has decreased and/or the density difference between the components has diminished. The mean squared electron density fluctuation, however, is model independent.

The data presented support a fibre microstructure that is two phase and remains two phase with increasing deformation. New crystalline regions are formed during the deformation, as indicated by the increase in degree of crystallinity. The microfibres become axially longer and

narrower, and are increasingly better oriented. The crystalline regions contain more defects with increasing deformation as evidenced by the decreased effective crystal density, ρ_c'. Lasch and Hsu have measured the average stem lengths for these three extrudated by Raman longitudinal acoustic mode (LAM) spectroscopy[43,50,51], using the LAM peak maximum. The number average stem length decreased from 230 Å–150 Å for 12 and 36 EDR, respectively (*Table 3*), while the breadth of the LAM peak increased, indicating a broadening of the distribution of stem lengths, including a tail of short stem lengths which has been associated with a substantial population of short chain extended segments. The decrease in the LAM stem length and the increase in the number of shorter stem lengths further indicates a substantial increase in the crystal defect content. The SAXS invariant decreases, but certainly does not vanish, even though the small-angle scattering long period peak intensity along the meridian decreases by a factor of 8 measured by peak height or 12 by peak area. A more reliable measure of the SAXS behaviour, rather than merely examining $\bar{L}$, is the mean squared electron density fluctuation, which is consistent in its decrease with EDR, with a 21% reduction from 12–36 EDR, and a 63% reduction from the initial billet material. The crystal size distribution (from dark field) becomes broader and the crystals are arranged in an increasingly non-periodic manner.

Consideration must also be given to the limits of the measurement of small-angle scattering. For polymer systems with large crystal sizes ($\geqslant$400 Å), a portion of the scattered intensity due to large periodicities (if any) is not observable by many instruments, and consequently is not sampled by this technique.

By assuming a two phase system with sharp boundaries (the latter assumption is verified by Porod analysis), the desired values of the effective noncrystalline phase density, ρ_a', are seen to initially increase from the unoriented amorphous density of 0.84 g cm^{-3} to a value of 0.89 g cm^{-3}, which is reasonable for a partially oriented, more densely packed noncrystalline arrangement of chains. This plateau in ρ_a' with EDR indicates that after initial formation of the oriented fibre structure further changes in the noncrystalline regions are not reflected in the density ρ_a'.

In order to make further use of SAXS, some model must be assumed,such as a sharp interface two phase system, which is often used for semicrystalline polymers. Sharp interfaces are verifiable from a Porod analysis which is anisotropic for an oriented system. The subtraction of the fluctuation scattering from the total scattering allows the determination of the densities of the two phases (now each of uniform density). The two phase model itself is not directly verifiable, but provides a self consistent picture, yielding a direct measure of ρ_a' unavailable for anisotropic samples from any other technique. To further assess the nature of the amorphous phase it would be necessary to measure heat capacity, or use n.m.r. or i.r. to probe the mobile chain fraction.

The levelling off of ρ_a' with EDR is in agreement with studies of the dependence of transport properties of drawn semicrystalline polymers with draw ratio. Williams and Peterlin[52] found that for linear polyethylene drawn at 60°C, the sorption and diffusion constants of methylene chloride dropped drastically between $\lambda = 8$ and 9, and then remained nearly constant up to $\lambda = 25$. Later studies[53] on low density polyethylene showed a similar trend, although the highest draw ratios obtained were $\lambda = 6$. Since the transport behaviour is dominated by the amorphous phase, the techniques used are very sensitive to the nature of the noncrystalline component. On drawing, the system is transformed from spherulitic-lamellar with a high permeability amorphous matrix to a fibrillar system containing a densified, lower permeability amorphous phase.

Transport properties (i.e. diffusion rate of small molecules), birefringence, infra-red dichroism and thermal expansion all provide information about the noncrystalline component in high modulus polyethylene. It is well established that the noncrystalline chain orientation increases with draw ratio, reaching a plateau above about 12 EDR. Since crystallite orientation also does not increase significantly at high draw ratios, the continued increase in modulus does not correlate well with chain orientation in either phase.

Ito[15] examined the noncrystalline phase in solid state extruded polyethylene by n.m.r., and found for 12 EDR or lower, three relaxation times which were associated with rigid (crystal), intermediate and noncrystalline components. At EDR of 25 or larger, only the crystalline and noncrystalline components were observed. The constraint on the noncrystalline component increased rapidly up to 12 EDR and reached a plateau above 12 EDR, in parallel to the degree of orientation of the noncrystalline chains, measured by birefringence[9,54] and thermal expansion coefficient[54].

Peterlin's model explains the increase in modulus with increasing draw ratio on a molecular basis: fibres are composed of microfibres with axially alternating regions of crystalline (folded chain lamellar crystals) and noncrystalline chains. The crystals are connected by a population of tie molecules running through the noncrystalline regions, and the tie molecules at the lateral edges of the microfibres are taut or even crystallized. Further drawing increases the number of taut tie molecules by decreasing the microfibril diameter through shearing and extension of the folded chains, thereby increasing modulus. One aspect of Peterlin's model is that the structure of the noncrystalline regions does not change significantly with draw at high draw ratios[47,55]. The decrease in segmental mobility and the increase in chain orientation, coupled with the initial densification of the noncrystalline phase up to 12 EDR and saturation above 12 EDR all lend support to Peterlin's two phase model. The molecular arrangement in the noncrystalline phase changes little at high draw ratios. The crystalline fraction is constant or increases slightly, reflecting conversion of folded chains to more extended chains which can crystallize. But the noncrystalline regions resist further densification so the system must respond to the applied stress by microfibre shear and/or crystal deformation.

The Ward model[19], like any series arrangement of structural elements, relies on the size estimate of a microstructural element from a global measurement technique (SAXS). However, when one of the critical parameters needed is based upon the long period, and in the situation when the intensity of the long period and hence the periodic fraction of the material is low, the validity of the model must be questioned.

An ideally periodic structure with single valued crystal

and noncrystal lengths would produce an interference peak (long period) that is completely representative of the structure. An assessment of the ideality of such a periodic model can be made from an inspection of the SAXS intensity (in the long period region) and of the crystal size distribution from electron microscopy and wide-angle X-ray scattering. For the 12 EDR sample, which exhibits relatively strong SAXS long period intensity, the periodicity is good, and the breadth of the long period peak is indicative of a narrow macrolattice size distribution. The crystal size distribution is relatively narrow as measured from dark field electron microscopy, and a periodic model is reasonable. But at 36 EDR, such an ideal periodic structure is certainly nonrepresentative. Rather, there is a broader crystallite size distribution containing a small component of very long crystals (1000–8000 Å), with sequences of diffracting crystallites (colonies) indicating the presence of thin intercrystalline bridges[18].

In Ward's intercrystalline bridge model, the parameter p is defined as the 'area fraction of intercrystalline bridge material which traverses the disordered layer'[19] and is determined by:

$$p = \frac{\bar{l}_c - \bar{L}}{\bar{l}_c + \bar{L}} \tag{15}$$

This definition is only useful for cases where $\bar{l}_c/\bar{L} > 1$ otherwise p is either zero or negative. This limits the applicability of this model, and in the present case, *Table 3* indicates that $\bar{l}_c/\bar{L}$ is less than one at 12 EDR and barely exceeds one at 24 EDR where the modulus is already 27 GPa! At 36 EDR the Ward model might appear to be reasonable, but the long period scattering peak is very weak indicating a very small amount of periodic structure (some material recrystallized at large undercooling for the high pressure extrusion?). Models that rely on the long period as a fundamental parameter, particularly for quantitative prediction of mechanical properties, must be reconsidered with the view that the long period although easily determined is not always a truly meaningful or appropriate average measure of the microstructure.

CONCLUSIONS

1. The use of a two phase model for solid state extruded polyethylene fibres is found to be justified if consideration is given to the effective densities ρ_c' and ρ_a' of the phases, which change with deformation. Use of nonperturbed density values for a deformed system is invalid. Effective densities can be obtained by careful application of wide and small-angle X-ray scattering methods for anisotropic systems.

2. The average axial crystallite length (lower bound) measured by wide-angle X-ray scattering increases with extrusion draw ratio, while the SAXS invariant and long period decrease. The effecitve density of the noncrystallinc component increases rapidly with draw ratio up to about 12, then remains constant (at 0.89 g cm^{-3}) with further draw to 36 EDR.

3. These extensive morphological observations involving both microscopy and X-ray techniques on a series of solid state extrudates are fully consistent with the key features of the Peterlin model of fibre microstructure.

ACKNOWLEDGEMENTS

The authors thank Dr J. S. Lin and Dr P. Labarbe of the ORNL NCSAR for many helpful discussions and for helping keep the 10 m SAXS system running during the lengthy measurements. Discussions were also fruitful with Dr S. L. Hsu and Mr J. Lasch concerning Raman LAM spectroscopy, and with Dr Dale Handlin (Shell Development Corp.) concerning small-angle scattering. The help in WAXS diffractometry by Ms C. Peschek at the University of Minnesota is gratefully acknowledged. Financial support was provided by the NSF through grants DMR 77-24955, 80-12725 (ELT) Polymers Program and grant CPE-8006348 (RSP) Chemical and Process Engineering and the Materials Research Laboratory of the University of Massachusetts.

REFERENCES

1 Southern, J. H. and Porter, R. S. *J. Macromol. Sci., Phys.*, 1970, **4**, 541
2 Imada, K. and Takayanagi, M. *Int. J. Polym. Mater.*, 1973, **2**, 89
3 Tsurata, A., Kamamoto, T., Tanaka, K. and Porter, R. S. *Polym. Eng. Sci.* 1983, **23**, 521
4 Capaccio, G., Clements, J., Hine, P. J. and Ward, I. M. *J. Polym. Sci., Polym. Phys. Edn.* 1981, **19**, 1435
5 Kanamoto, T., Tsuruta, A., Tanaka, K., Takeda, M. and Porter, R. S. *Rep. Prog. Polym. Phys. Jpn.* 1983, **26**, 347
6 Sakurada, I., Ito, T. and Nakamai, K. *J. Polym. Sci.* 1966, **C15**, 75
7 Shimanouchi, T., Asahina, M. and Enomoto, S. *J. Polym. Sci.* 1962, **59**, 93
8 Muruyama, S., Imada, K. and Takayanagi, M. *Int. J. Polym. Mat.* 1973, **2**, 105
9 Nakayama, K. and Kanetsuna, H. *J. Mater. Sci.* 1975, **10**, 1105
10 Kolbeck, A. G. and Uhlmann, D. R. *J. Polym. Sci., Polym. Phys. Edn.* 1979, **17**, 421
11 Kanamoto, T., Zachariades, A. E. and Porter, R. S. *Polym. J.* 1979, **11**, 307
12 Kanamoto, T., Fujimatsu, S., Tsuruta, A., Tanaka, K. and Porter, R. S. *Rep. Prog. Polym. Phys. Jpn.* 1981, **24**, 185
13 Maeda, Y., Nakayama, K. and Kanetsuna, H. *Polym. J.* 1982, **14**, 649
14 Clements, J., Jakeways, R. and Ward, I. M. *Polymer* 1978, **19**, 639
15 Ito, M., Kanamoto, T., Tanaka, K. and Porter, R. S. *Macromolecules* 1981, **14**, 1779
16 Zachariades, A. E., Mead, W. T. and Porter, R. S. *Chem. Rev.* 1980, **80**, 351
17 Clark, E. S. and Scott, L. S. *Polym. Eng. Sci.* 1974, **14**, 682
18 Sherman, E. S., Porter, R. S. and Thomas, E. L. *Polymer* 1982, **23**, 1069
19 Gibson, A. G., Davies, G. R. and Ward, I. M. *Polymer* 1978, **19**, 683
20 Wu, W., Simpson, P. G. and Black, W. B. *J. Polym. Sci., Polym. Phys. Edn.* 1980, **18**, 751
21 Dismore, P. F. and Statton, W. O. *J. Polym. Sci. Part C* 1966, **13**, 133
22 Slutsker, A. I., Sanphirova, T. P., Yastrebenskii, A. A. and Kuksenko, V. S. *J. Polym. Sci. Part C* 1968, **16**, 4093
23 Statton, W. O. *J. Polym. Sci. A2* 1972, **10**, 1587
24 Peterlin, A. and Corneliussen, R. *J. Polym. Sci. A-2* 1968, **6**, 1273
25 Dumbleton, J. H. and Buchanan, D. R. *J. Polym. Sci. A-2* 1968, **6**, 1527
26 Dumbleton, J. H. *J. Polym. Sci. A-2* 1969, **7**, 667
27 Prevorsek, D. C., Tirpak, G. A., Harget, P. J. and Reimschuessel, A. C. *J. Macromol. Sci. Phys.* 1974, **B9**, 733
28 Hermans, P. H. and Weidinger, A. *Makromol. Chem.* 1960, **39**, 67
29 Fischer, E. W., Goddar, H. and Schmidt, G. F. *Makromol. Chem.* 1968, **118**, 144
30 Kavesh, S. and Schultz, J. M. *J. Polym. Sci. A-2* 1971, **9**, 85
31 Sakaoku, K., Morosoff, N. and Peterlin, P. *J. Polym. Sci. Polym. Phys. Edn.* 1973, **11**, 31
32 Matyi, R. J. and Crist, Jr., B. *J. Polym. Sci. Polym. Phys. Edn.* 1978, **16**, 1329
33 Rachinger, W. A. *J. Sci. Instrum.* 1948, **25**, 254
34 Klug, H. P. and Alexander, L. E. in 'X-Ray Diffraction Pro-

cedures for Polycrystalline and Amorphous Materials', John Wiley and Sons, London (1974)
35 Stokes, A. R. and Wilson, A. J. C. *Proc. Camb. Phil. Soc.* 1944, **40**, 197
36 Hendricks, R. W. *J. Appl. Cryst.* 1978, **11**, 15
37 Luzzati, V. *Acta Cryst.* 1960, **13**, 939
38 Porod, G. *Kolloid-Z.* 1951, **124**, 83
39 Adams, W. W., Handlin, D. L. and Thomas, E. L. to be published
40 Alexander, L. E. in 'X-Ray Diffraction Methods in Polymer Science' (1969), reprinted by R. E. Krieger Pub. Co., New York (1979)
41 Fischer, E. W. and Fakirov, S. *J. Mater. Sci.* 1976, **11**, 1041
42 Hamzeh, F. M. and Bragg, R. H. *J. Appl. Phys.* 1974, **45**, 3189
43 Lasch, J. E. and Hsu, S. L. *Polym. Prepr., Am. Chem. Soc., Div. Polym. Chem.* 1981, **22(2)**, 337
44 Fischer, E. W. and Schmidt, G. F. *Angew. Chem. Int. Ed. Engl.* 1962, **1**, 488
45 Corneliusson, R. and Peterlin, A. *Makromol. Chem.* 1967, **105**, 193
46 Crist, B. *J. Appl. Cryst.* 1979, **12**, 27
47 Peterlin, A. *Polym. Eng. Sci.* 1977, **17**, 183
48 Rathje, J. and Ruland, W. *Colloid Polym. Sci.* 1976, **254**, 358
49 Wiegand, W. and Ruland, W. *Prog. Colloid Polym. Sci.* 1978, **64**, 147
50 Wang, Y. K., Waldman, D., Lasch, J. E., Stein, R. S. and Hsu, S. L. *Macromolecules* 1982, **15**, 1452
51 Lasch, J. private communication
52 Williams, J. L. and Peterlin, A. *J. Polym. Sci.: Part A-2* 1971, **9**, 1483
53 DeCandia, F., Russo, R., Vittoria, V. and Peterlin, A. *J. Polym. Sci., Polym. Phys. Edn.* 1980, **18**, 2083
54 Mead, W. T., Desper, C. R. and Porter, R. S. *J. Polym. Sci., Polym. Phys. Edn.* 1979, **17**, 859
55 Peterlin, A. *J. Mater. Sci.* 1971, **6**, 490